Peer-reviewed version available at Water 2019, 11, 1444; doi:10.3390/w11071444

Article

Secondary flow effects on deposition of cohesive sediment in a meandering reach of Yangtze River

Cuicui Qin [1,*], Xuejun Shao [1] and Yi Xiao [2]

[1] State Key Laboratory of Hydroscience and Engineering, Tsinghua University, Beijing 100084, China; qincuicui2009@163.com; shaoxj@mail.tsinghua.edu.cn
[2] National Inland Waterway Regulation Engineering Research Center, Chongqing Jiaotong University, Chongqing, China; xymttlove@163.com
* Correspondence: qincuicui2009@163.com; Tel.: +86-188-1137-0675 (F.L.)

Received: date; Accepted: date; Published: date

Abstract: A conventional 2D numerical model is improved by incorporating three submodels to consider different effects of secondary flow and a module for cohesive sediment transport. The model is applied to a meandering reach of Yangtze River to investigate secondary flow effects on cohesive sediment deposition, and a preferable submodel is selected based on the flow simulation results. Sediment simulation results indicate that the improved model predictions are in better agreement with the measurements in planar distribution of deposition as the increased sediment deposits caused by secondary current on the convex bank have been well predicted. Secondary flow effects on predicted amount of deposition become more obvious during the period when the sediment load is low and velocity redistribution induced by the bed topography is evident. Such effects vary with the settling velocity and critical shear stress for deposition of cohesive sediment. The bed topography effects can be reflected by the secondary flow submodels.

Keywords: secondary flow; cohesive; deposition; 2D numerical model; meandering; Yangtze River

1. Introduction

Helical flow or secondary flow caused by centrifuge force in meandering rivers plays an important role in flow and sediment transport. It redistributes the main flow and sediment transport, mixes dissolved and suspended matter, causes additional friction losses and additional bed shear stress which are responsible for the transverse bedload sediment transport [1-3]. Moreover, the secondary flow may affect lateral evolution of river channels [4-6]. Extensive researches have been conducted about secondary flow effects on flow and sediment transport, especially bed load in a singular bend [7] or meandering channels of laboratory scale [8] and rivers of field scale [9,10]. However, few researches focus on suspended load transport. In China, sediment transport in most rivers is dominated by suspended load, such as Yangtze River and Yellow River. On the Yangtze River, the medium diameter of sediment from upstream is about 0.01 mm [11] which has taken on cohesive properties to some extent [11,12]. More importantly, these cohesive suspended sediments have been extensively deposited in several reaches which have blocked the waterway in Yangtze River [13]. As most of these reaches are meanders with a central bar located in the channel, to what extent the secondary flow has affected the cohesive suspended sediment deposition should be investigated.

Cohesive sediment deposition is controlled by bed shear stress [14], which is determined by the flow field. In order to investigate the secondary flow effects on cohesive sediment transport, its effects on flow field should be considered first. Secondary flow redistributes velocities, which means the high velocity core shifts from the inner bank to the outer bank of the bend [15,16]. Saturation of secondary flow takes place in sharp bends [17]. Due to the inertia, the development of secondary flow lags behind the curvature called the phase lag effect [18]. All these findings mainly rely on laboratory experiments or small rivers with a width to depth radio less than 30 [19]

probably resulting in an exaggeration of secondary flow. When it comes to natural meandering or anabranching rivers, especially large or mega rivers, secondary flow may be absent or limited in a localized portion of the channel width [20-24]. However, those researches are only based on field surveys and mainly focused on influences of bifurcation or confluence of mega rivers with low curvatures and significant bed roughness [23] at the scale of individual hydrological events. On contrary, Nicholas [25] emphasized the role of secondary flow played in generating high sinuosity meanders via simulating a large meandering channel evolution on centennial scale. Maybe it depends on planimetric configurations, such as channel curvature, corresponding flow deflection [26] and temporal scales. Therefore, whether secondary flow exists and has the same effects on the flow field in a meandering mega river as that in laboratory experiments should be further investigated. Besides, the long-term hydrograph should be taken into account.

As to its effects on bed morphology, secondary flow induced by channel curvature produces a point bar and pool morphology by causing transversal transport of sediment, which in turn drives lateral flow (induced by topography) known as topographic steering [9] which plays an even more significant role in meandering dynamics than that curvature-induced secondary flow [3]. The direction of sediment transport is derived from that of depth-averaged velocity due to the secondary flow effect, which has been accounted for in 2D numerical models and proved to contribute to the formation of local topography [4-6,27], especially bar dynamics [28,29] and even to channel lateral evolution [4,6,30]. Although Kasvi et al. [31] has pointed that the exclusion of secondary flow has a minor impact on the point bar dynamics, temporal scale effects remain to be investigated as the authors argued for only one flood event has been considered in their research and the inundation time may affect the effects of secondary flow [32]. Those researches have enriched our understandings of mutual interactions of secondary flow and bed morphology. However, they mainly focused on bed load sediment transport whereas the world largest rivers are mostly fine-grained system [21] and even dominated by silt and clay such as Yangtze River [11,12]. Fine-grained suspended material ratio controls the bar dynamics and morphodynamics in mega rivers [23,33]. As is known, such fine-grained sediment is common in estuarine and coastal areas. However, how they work under the impacts of secondary flow in mega rivers is still up in the air.

Numerical method provides a convenient tool for understanding river evolution in terms of hydrodynamics and morphodynamics in addition to the laboratory experiments and field surveys. By comparison with 3D and 1D models, 2D model keeps as much detailed information as possible on the one hand and remains practical for investigation of long-term and large-scale fluvial processes on the other hand. However, as for 2D model, the vertical structure of flow is lost due to the depth-integration of the momentum equations so that the secondary flow effects on flow field are neglected. In order to account for these effects in 2D models, various correction submodels have been proposed by many researchers [34-38]. The differences among these models are whether or not they consider 1) the feedback effects between main flow and secondary flow, and 2) the phase lag effect of the secondary flow caused by inertia. Models neglecting the former one are classified as linear models, in contrast to nonlinear models which consider such effects [1,38]. The nonlinear models [1,39] based on the linear ones are more suitable for flow simulation of sharp bends [1,2]. The phase lag effect which is obviously pronounced in meandering channels [40] has been thought to be important in sharp bends especially with pronounced curvature variations [2] and proven to influence bar dynamics considerably [29]. Although the performances of those above mentioned models have been extensively tested by laboratory scale bends, their applicability to field meandering rivers, especially mega rivers, needs to be further investigated.

In addition, the lateral transport of suspended sediment caused by secondary flow should be incorporated into 2D models. However, as to the cohesive sediment transport, it is mainly related to the bed shear stress determined by the flow field. Besides, according to field survey of two reaches of Yangtze River by Li et al. [11], cohesive sediment transport is controlled by the depth-averaged velocity. Therefore, only the secondary flow effects on flow field are considered to further analyze their effects on bed morphology here.

Overall, three questions arise based on the above review: (1) whether secondary flow effects can be reflected by secondary flow models on flow field in such mega meandering rivers; (2) which model should be given priority to flow simulation in meandering channels of such scale; (3) what the temporal influence of secondary flow is on bed morphology variations associated with cohesive sediment deposition. In order to address these questions, three secondary flow submodels referring to the aforementioned different effects have been selected from the literature, Lien et al. [37], Bernard [35] and Blankaert and de Vriend [1] models, to reveal secondary flow impacts and distinguish their performances on flow simulation in meandering channels of this mega scale firstly. And the preferable model is selected. Then, the corresponding model is applied to investigate secondary flow effects on bed morphology variations related with cohesive sediment deposition during an annual hydrograph. Finally, the correction terms representing secondary flow effects have been analyzed to justify their functionalities and performances of these models in meandering channels of such scale. Besides, the roles of cohesive sediment played in secondary flow effects have been investigated as well.

2. Methods

A conventional 2D numerical model (2.1, referred to as the N model hereafter) has been improved by considering secondary flow effects and cohesive sediment transport. Secondary flow module (2.2) incorporates three different submodels to reflect its different effects, together with the sediment module (2.3) are described briefly. All the equations are solved in orthogonal curvilinear coordinates.

2.1 Flow equations

The unsteady 2D depth-averaged flow governing equations are expressed as follows [41].

$$\frac{\partial Z}{\partial t}+\frac{1}{J}\left[\frac{\partial(h_2HU)}{\partial\xi}+\frac{\partial(h_2HV)}{\partial\eta}\right]=0 \tag{1}$$

$$\frac{\partial(HU)}{\partial t}+\frac{1}{J}\left[\frac{\partial(h_2HUU)}{\partial\xi}+\frac{\partial(h_1HVU)}{\partial\eta}\right]-\frac{HVV}{J}\frac{\partial h_2}{\partial\xi}+\frac{HUV}{J}\frac{\partial h_1}{\partial\eta}+\frac{gH}{h_1}\frac{\partial Z}{\partial\xi}+\frac{HUg\left|H\vec{u}\right|}{(CH)^2}=\frac{\upsilon_e H}{h_1}\frac{\partial E}{\partial\xi}-\frac{\upsilon_e H}{h_2}\frac{\partial F}{\partial\eta}-S_\xi \tag{2}$$

$$\frac{\partial(HV)}{\partial t}+\frac{1}{J}\left[\frac{\partial(h_2HUV)}{\partial\xi}+\frac{\partial(h_1HVV)}{\partial\eta}\right]+\frac{HUV}{J}\frac{\partial h_2}{\partial\xi}-\frac{HUU}{J}\frac{\partial h_1}{\partial\eta}+\frac{gH}{h_2}\frac{\partial Z}{\partial\eta}+\frac{HUg\left|H\vec{u}\right|}{(CH)^2}=\frac{\upsilon_e H}{h_1}\frac{\partial E}{\partial\eta}-\frac{\upsilon_e H}{h_2}\frac{\partial F}{\partial\xi}-S_\eta \tag{3}$$

$$E=\frac{1}{J}\left[\frac{\partial(h_2U)}{\partial\xi}+\frac{\partial(h_1V)}{\partial\eta}\right]\quad F=\frac{1}{J}\left[\frac{\partial(h_2V)}{\partial\xi}-\frac{\partial(h_1U)}{\partial\eta}\right] \tag{4}$$

where ξ and η = longitudinal and transverse direction in orthogonal curvilinear coordinates respectively; h_1 and h_2 = metric coefficients in ξ and η directions respectively; $\vec{u}$ = depth-averaged resultant velocity vector; H = water depth; Z = water surface elevation; C = Chezy factor; ν_e = eddy viscosity; S_ξ and S_η = correction terms related to the vertical non-uniform distribution of velocity; (U, V) = depth-averaged velocity in ξ and η directions separately.

2.2 Secondary Flow equations

In order to consider different effects of secondary flow on flow, three secondary flow models are selected from literature to calculate the dispersion terms (S_ξ, S_η) in Equation (2 ~ 3). Among them, Lien et al. [37] (L) model has been widely applied, which ignore the secondary flow phase lag effect and is suitable for fully developed flows. As secondary flow lags behind the driving curvature due to inertia [2], it will take a certain distance for secondary flow to fully develop, especially in meandering channels. There are several models using a depth-averaged transport equation to consider these phase lag effect, such as Delft-3D [42] model, Hosoda et al. [43] model and Bernard [35] model. Delft-3D model has two correction coefficients to calibrate and Hosoda model is complex to use. In addition, both of them focus on flow simulation in channels with a single bend. In contrast, Bernard (B) model is simple and practicable which has been validated by

several meandering channels. Moreover, the sidewall boundary conditions considered by B model is more reasonable, that is, the production of secondary flow approaches zero on the sidewalls [16]. Therefore, the B model is selected as another representative model. Because the above mentioned two models are linear models which are theoretically only applicable to mildly curved bends, a simple nonlinear (NL) model [1] is selected as a typical model to reflect the saturation effect of secondary flow [17] in sharply curved bends. All of the three models can reflect the velocity redistribution phenomenon caused by secondary flow at different levels. These models serve as submodels coupled to the 2D hydrodynamic model to account for different effects of secondary flow on flow field. The major differences of them are summarized in Table 1, while L and B models can refer to the authors [44] for more details. Only NL model are briefly described as follows.

Based on linear models, NL model is able to consider the feedback effects between secondary flow and main flow to reflect the saturation effect through a bend parameter β [1] (Equation 10). However, NL model proposed by Blanckaert and de Vriend [1] is limited to the centerline of the channel. Ottevanger [45] extended the model to the whole channel width through an empirical power law (f_w, Equation 9). This method is as follows.

$$S_\xi = \frac{1}{J}\frac{\partial}{\partial \xi}(h_2 T_{11}) + \frac{1}{J}\frac{\partial}{\partial \eta}(h_1 T_{12}) + \frac{1}{J}\frac{\partial h_1}{\partial \eta}T_{12} - \frac{1}{J}\frac{\partial h_2}{\partial \xi}T_{22} \quad (5)$$
$$S_\eta = \frac{1}{J}\frac{\partial}{\partial \xi}(h_2 T_{12}) + \frac{1}{J}\frac{\partial}{\partial \eta}(h_1 T_{22}) - \frac{1}{J}\frac{\partial h_1}{\partial \eta}T_{11} + \frac{1}{J}\frac{\partial h_2}{\partial \xi}T_{12}$$

$T_{i,j}$ (i, j =1,2) is called dispersion terms [37]. When L model is adopted as the linear model, $T_{i,j}$ is expressed as :

$$T_{11} = HUU\left(\frac{\sqrt{g}}{\kappa C}\right)^2 \quad T_{12} = T_{21} = HUV\left(\frac{\sqrt{g}}{\kappa C}\right)^2 + f_{sn}(\beta) f_w \frac{(HU)^2}{\kappa^2 r}\frac{\sqrt{g}}{\kappa C} FF1 \quad (6)$$
$$T_{22} = HVV\left(\frac{\sqrt{g}}{\kappa C}\right)^2 + f_{sn}(\beta) f_w \frac{2HUHV}{\kappa^2 r}\frac{\sqrt{g}}{\kappa C} FF1 + f_{nn}(\beta) f_w^2 \frac{(HU)^2 H}{\kappa^4 r^2} FF2$$

where $f_{sn}(\beta)$ and $f_{nn}(\beta)$ are the nonlinear correction coefficients expressed as Equation (7 ~ 8) [46] which directly reflect the saturation effect of secondary flow [17]. Other parameters, κ = the Von Karman constant, 0.4; r = the channel centerline, m; f_w = the empirical power law equation over the channel width; *FF1*, *FF2* = the shape coefficients related to the vertical profiles of velocity which can refer to [37] for details.

$$f_{sn}(\beta) = 1 - \exp\left(-\frac{0.4}{\beta(\beta^3 + 0.25)}\right) \quad (7)$$

$$f_{nn}(\beta) = 1.0 - \exp\left(-\frac{0.4}{1.05\beta^3 - 0.89\beta^2 + 0.5\beta}\right) \quad (8)$$

$$f_w = \left[1 - \left(\frac{2n}{w}\right)^{2n_p}\right] \quad (9)$$

$$\beta = C_f^{-0.275}(H/R)^{0.5}(1+\alpha)^{0.25} \quad (10)$$

$$\alpha_s = \left[w\partial U_s/\partial n/U_s\right]_{n_c} \quad (11)$$

β = the bend parameter which is a control parameter distinguishing the linear and nonlinear models; α_s = the normalized transversal gradient of the longitudinal velocity U at the centerline; n_c = the position of channel centerline.

The phase lag effect of secondary flow is considered with the following transport equations [45].

$$\frac{1}{J}\left[\frac{\partial(h_2 HUY)}{\partial \xi} + \frac{\partial(h_1 HVY)}{\partial \eta}\right] = \frac{h|\vec{u}|}{\lambda}(Y_e - Y) \quad (12)$$

λ = the adaption length described by Johannesson and Parker [18]. Y = the terms referring to f_{sn}, f_{nn} in Equation 6, Y_e = the fully developed value of Y.

Table 1. Differences between L, B and NL models.

	L model	B model	NL model
Saturation effect	NO	NO	YES
Phase lag effect	NO	YES	YES
Wall boundary condition	-	no secondary flow produced	dispersion terms = 0
Velocity redistribution	YES	YES	YES

As L, B and NL models serve as closure submodels in hydrodynamic equations (1 ~ 4), the correction terms (S_ξ, S_η) are associated with the computed mean flow field, and the information on the relative variables of correction terms is available when solving these submodels. This is similar to the way to solve turbulence submodels. Detailed procedure for solving the NL model is shown in Figure 1. Equation (1 ~ 4) are solved first without considering the correction terms (S_ξ, S_η) for water depth and depth-averaged velocity. The nonlinear parameters in Equation (7 ~ 11) have been calculated next. Afterwards, the transport equation (12) is solved for evaluating dispersion terms ($T_{i,j}$, Equation 6) and (S_ξ, S_η) (Equation 5). The correction terms (S_ξ, S_η) are then included in Equation (1 ~ 4) which are solved again to get new information on the mean flow field. The procedure continues until no significant variations in the magnitude of depth, velocity and other variables in the model. (Figure 1).

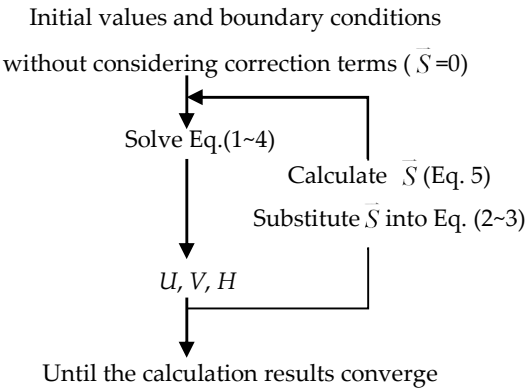

Figure 1. Solution procedure.

2.3 Cohesive Sediment Transport Equations

The cohesive sediment transport equation is similar to the noncohesive sediment transport equation [47], except the method to calculate the net exchange rate (D_b-E_b) [14].

$$\frac{\partial(HC)}{\partial t}+\frac{1}{J}\left[\frac{\partial(h_1HCU)}{\partial\xi}+\frac{\partial(h_1HCV)}{\partial\eta}\right]-\frac{H\varepsilon}{J}\left[\frac{\partial}{\partial\xi}\left(\frac{h_2}{h_1}\frac{\partial C}{\partial\xi}\right)+\frac{\partial}{\partial\eta}\left(\frac{h_1}{h_2}\frac{\partial C}{\partial\xi}\right)\right]+D_b-E_b=0 \quad (13)$$

where C = the sediment concentration, kg·m^{-3}; D_b, E_b = the erosion and deposition rate respectively, kg·m^{-2}·s^{-1}, which are calculated [14] as follows.

$$D_b=\alpha\omega_s C \quad (14)$$

where α = deposition coefficient calculated by Equation (15); ω_s = settling velocity, m·s^{-1}.

$$\alpha = \begin{cases} 1 - \dfrac{\tau_b}{\tau_{cd}}, \tau_b \le \tau_{cd} \\ 0, \tau_b > \tau_{cd} \end{cases} \quad (15)$$

where τ_b = the bed shear stress, Pa; τ_{cd} = the critical shear stress for deposition, Pa.

$$E_b = M\left(\frac{\tau_b}{\tau_{ce}}\right)^n \quad \tau_b > \tau_{ce} \quad (16)$$

where n = an empirical coefficient; M = the erosion coefficient, kg·m^{-2}·s^{-1}; τ_{ce} = the critical shear stress for erosion, Pa.

Most of the model parameters used for cohesive sediment calculation (Table 2) have been calibrated and validated by the sedimentation process of the Three Gorges Reservoir on Yangtze River [47], where the study area of this paper is located. A larger value of settling velocity is chosen from measurements by Li et al. [11,12] because only the medium diameter of the sediment is considered in this study.

Table 2. Model parameters used for cohesive sediment calculation.

Related variables	values
Settling velocity ω_s	2.1 mm·s^{-1}
Critical shear stresses τ_{cd}, τ_{ce}	0.41 Pa
Erosion coefficient M	1.0×10^{-8} kg·m^{-2}·s^{-1}
Empirical coefficient n	2.5

The morphological evolution due to cohesive sediment transport is calculated by the net sediment exchange rate (D_b-E_b), in the same way as non-cohesive suspended sediment calculation does. The flow and sediment modules are solved in an uncoupled way. Details of the numerical method can be found in [41]. Central difference explicit scheme is applied to Equation (5), and Equations (12) and (13) are solved by QUICK finite difference scheme.

3. Study case

The Hunghuacheng reach (HHC, Figure 2), located 364 km upstream from the Three Gorges Project (TGP), is approximately 13 km long, consisting two sharply curved bends with a center bar named "Huanghuacheng" splitting the reach into two branches. It belongs to the back water zone of TGP. The large mean annual discharge (32000 m^3·s^{-1}) makes it a mega river reach [48]. Measurements of bed topographies and bed material size are taken at nine cross sections from S201 to S209 twice each year. Due to huge amount of cohesive sediment siltation, the left branch of this reach has been blocked in September 2010 [13]. Secondary flow models are applied to this reach because the secondary flow caused by the upstream bend of this reach plays an important role in channel morphodynamics [49,50]. Also, it has been shown that similar models perform well in confluence [38] and braided rivers [25], which justify the application of these models in this reach.

The year 2012 is selected to study the secondary flow effects on bed morphology variation in this reach because of the record amount of deposition that year. The inlet and outlet boundaries are S209 and S201, respectively (Figure 2). Inlet boundary conditions of incoming flow and sediment are interpolated from Qingxichang and Wanxian gauging stations, while water stage measured at Shibaozhai station is used as the outlet boundary condition (Figure 2). Only the flood season from May to November is simulated instead of a whole year because most sediment is transported during this period (Figure 3b), similar to the method applied by Fang and Rodi [51] to study the sedimentation of near dam region after TGP impoundment. This duration has been divided into six periods based on the water stage process (Figure 3a). It should be noted that the water stage rising during the last period of this process is resulted from the operation of TGP.

Preprints (www.preprints.org) | NOT PEER-REVIEWED | Posted: 28 May 2019 doi:10.20944/preprints201905.0336.v1

Peer-reviewed version available at Water 2019, 11, 1444; doi:10.3390/w11071444

A median size of 0.008 mm is used to represent the inflow cohesive sediment composition of this reach [13]. A flood event on July 16, 2012 is chosen as a verification case for this river reach simulation. Table 3 lists parameters and conditions of it. Because the radius to width ratio (r/w) is in the range of 0.8 ~ 2.0 (Table 3), this river reach belongs to sharply curved bends. The computation domain of the river reach is divided into 211×41 grids in longitudinal and transverse directions, with time steps of 1.0 s and 60.0 s for flow and sediment calculation respectively.

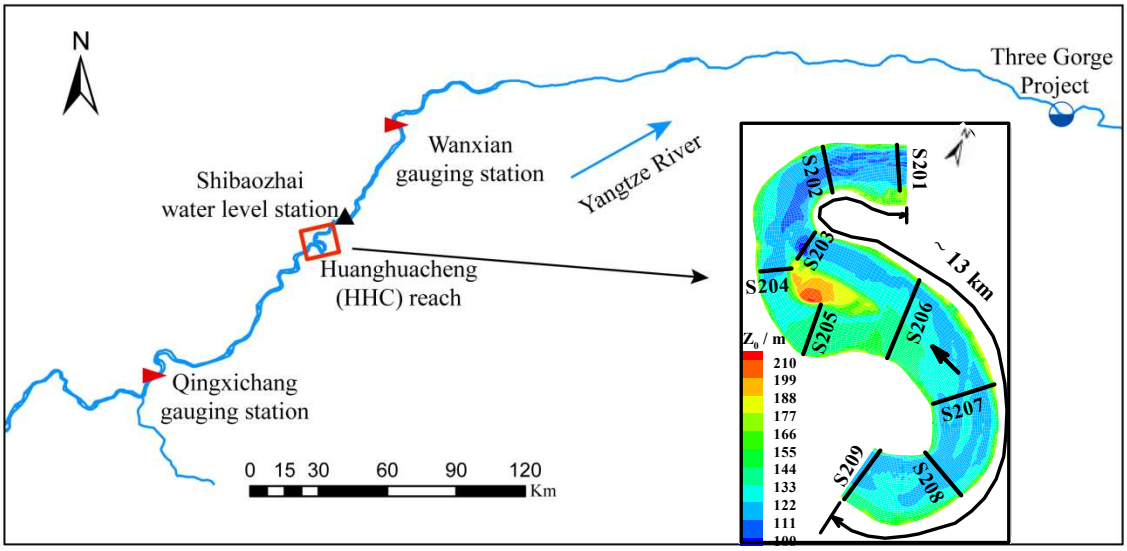

Figure 2. Planform geometry, bed elevation (Z_0) on March 2012 and nine cross sections measured in HHC reach (S209 and S201 are the inlet and outlet boundaries, respectively; Incoming flow discharge and sediment concentration used as inlet boundaries are interpolated from Qingxichang and Wanxian gauging station, located upstream 476.46 km and 291.38 km from TGP respectively, and the of outlet boundary applies the water stage measured at Shibaozhai station, located upstream 341.35 km from the TGP).

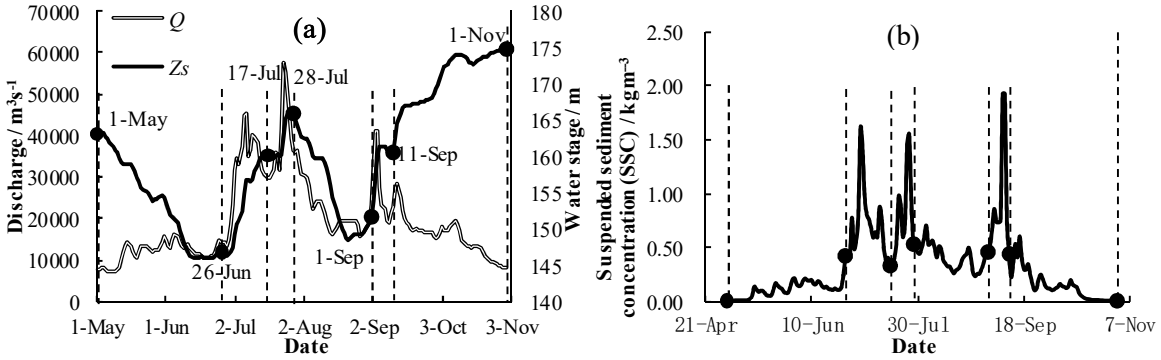

Figure 3. (a) Hydrograph and water stage from May 1 to November 1 (Q and Zs represent discharge and water stage respectively); the black filled circles divide the duration into several periods descripted clearly by the vertical black dash lines (b) Suspended sediment concentration (SSC) as the inlet boundary in this duration.

Table 3. Channel Dimensions and Flow Condition of HHC reach.

Study case	Discharge Q / m^3s^{-1}	Depth H / m	Width w / km	Bend radius r / km	r/w	H/r	Adaption length λ
HHC	30200	16 ~ 67	0.7 ~ 2.0	> 0.4	0.8 ~ 2.0	0.001 ~ 0.066	0.001 ~ 0.2

4. Results

The flow simulation results of L, B and NL models are verified for the discharge of 30200m^3·s^{-1} and the model with best performances has been selected. The preferable model L and the reference model N are used to predict cohesive sediment deposition during an annual hydrograph. The basic parameters, such as eddy viscosity coefficient and roughness of flow module, and parameters of sediment module are calibrated in N model first and then applied to the other models.

4.1. Verifications

4.3.1. Flow

Figure 4 shows simulated water stage at the right bank and the depth-averaged velocities across the channel width of the HHC reach. It is can be seen that the L model results are more reasonable than those of the other models. The velocity shift due to secondary flow can be well predicted by the L and B models at the end of the bends (S202 and S206), especially at the exit of the second bend (S202), in contrast to other models. In addition, as the high velocity core shifts to the right bank at the end of the first bend (S206), velocity of the left branches (S205) has been reduced. That explains why the velocities predictions by the B and L models are lower than those by N and NL models at S205 (Figure 4c). Overall, the differences between N and NL models are small, while L model are preferable according to the flow simulation results of the HHC reach.

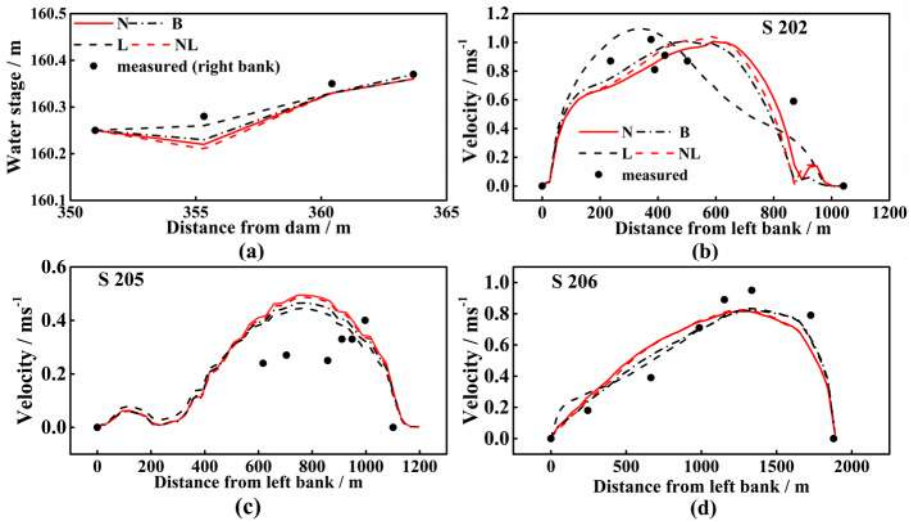

Figure 4. (a) Water stage of the right bank (downstream view); (b) (c) and (d) Depth-averaged velocity distribution measured and predicted by N, B, L and NL models at three cross sections for discharge 30200m^3·s^{-1}

4.3.2. Sediment

Based on the above flow simulation results, the L model has been applied to the HHC reach to investigate the secondary flow effects on cohesive sediment deposition. The results of N model serves as a reference.

The deposition module is verified by field measurements (Figure 5a) in terms of planar distribution of deposition (Figure 5b ~ 5c), bed elevation (Figure 6) and amounts of deposition. Figures 5a ~ 5c show that the simulated planar distribution of deposits by the L and N models agree with field measurements qualitatively, with the maximum thickness of deposits found at the convex bank of the first bend, and the majority of deposits located at the right bank of the inlet and the left branch of the reach. The predicted thickness of sediment deposits by the L model is approximately 1 m thicker than that by N model on the concave bank of the first bends (region 1, Figure 5d), which is much closer to the measurement 5 ~ 7 m (Figure 5a). Bed elevations simulated by the two models matches well with measurements at S204 ~ S206 (Figure 6). Predictions of total amounts of deposition from S206 to S203 are 8.33 ×10^6 m^3 and 8.0 × 10^6 m^3 by the N and L models respectively, while the field measurement during the same period is 8.18 ×10^6 m^3 [13]. The relative error is around

2 %, which qualify the sediment module used in this paper. In general, the L model performs better than the N model in predicting the planar distribution of cohesive sediment deposition.

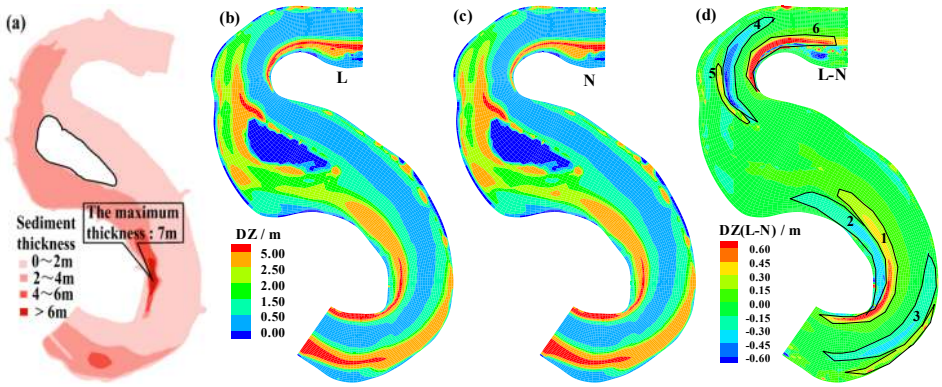

Figure 5. (a) Planar distribution of sediment thickness measured, the maximum is 7 m from March to August, 2012; (b) Sediment thickness simulated by the L model; (c) by the N model; (d) The difference between the L and N models.

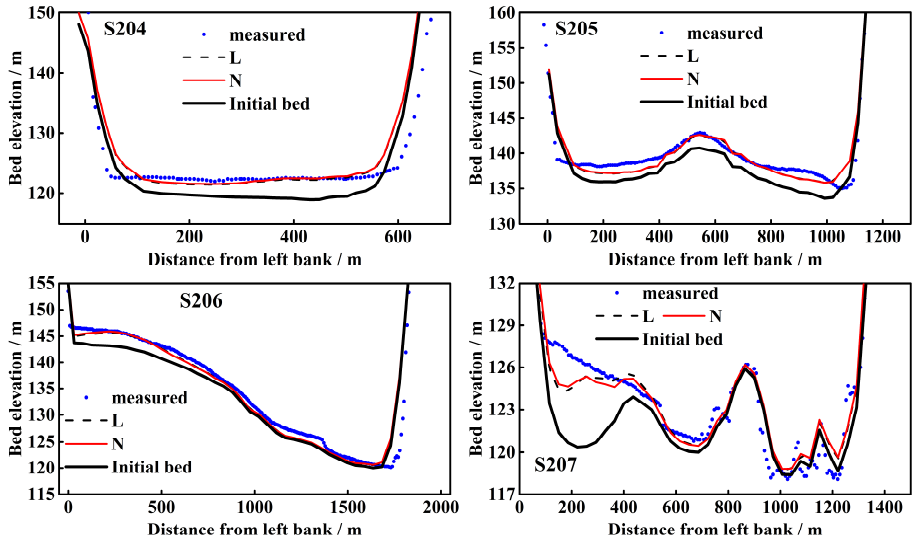

Figure 6. Comparison of bed elevation at cross sections between measurements and predictions.

4.2. Secondary Flow Effects on Cohesive Sediment Deposition

The differences in planar distribution and amounts of deposition predicted by the L and N models have been illustrated in Figure 5 (d) and Figure 7 respectively, which clearly suggest the secondary flow effects on cohesive sediment deposition. Due to its impacts, high velocity core shifts from the convex to the concave bank of the bend, leading to the redistribution of bed shear stress and the consequent morphological changes [9]. Shifts of high velocities predicted by the L model result in the more deposition in region 1, 5 and 6 and less deposition in region 3 and 4. The increase of sediment deposits in region 1 reduces sediment transported to region 2, resulting in less deposition here. The difference of predicted amount of deposition between the two models is about $0.31 \times 10^6 m^3$ from September 11 to November 1, as clearly shown in Figure 7. This difference is small compared to the total amount of deposition during the whole year, approximately 8.0×10^6 m^3. However, this difference can accumulate if the water stage keeps rising due to the impoundment of TGP. In general, secondary flow effects on cohesive sediment deposition become more obvious in the last period of the annual hydrograph when the sediment load is low and water stage is high (Figure 3).

The total deposition volume is calculated from S203 ~ S206 during different periods of this year, because this part of the reach is seldom affected by the inlet and outlet boundaries. Deposition of this part is greatly impacted by the velocity redistribution at S206 (e.g. Figure 4c and 4d), which is

controlled by the secondary flow produced in the upstream bend and the bed topography (transverse bed slope) there. In addition, the sediment load plays an important role in the deposition of this part. Therefore, the average of suspended sediment load during different periods has been shown in Figure 7 as well. When the sediment load is low, the velocity redistribution plays a dominate role resulting in more sediment transport downstream and less deposition due to the shift of high velocities to the right branch. Otherwise, the situation is just reversed, and more deposits can occur in the left branch resulting from the huge amount of sediment transported, despite of the fact that the velocities are higher in the right branch. These can qualitatively explain the difference in predicted amounts of deposition during different periods except the fifth period (September 1 ~ 11). In that period, the transverse bed slope at S206 is high enough to strengthen velocity redistribution further, thus surpasses the effects of higher sediment load and result in less predicted deposition by the L model than the N model. During the last period (September 11 ~ November 1), the significant difference of predicted deposition volume is resulted from both the low sediment load transport and the large transverse bed slope.

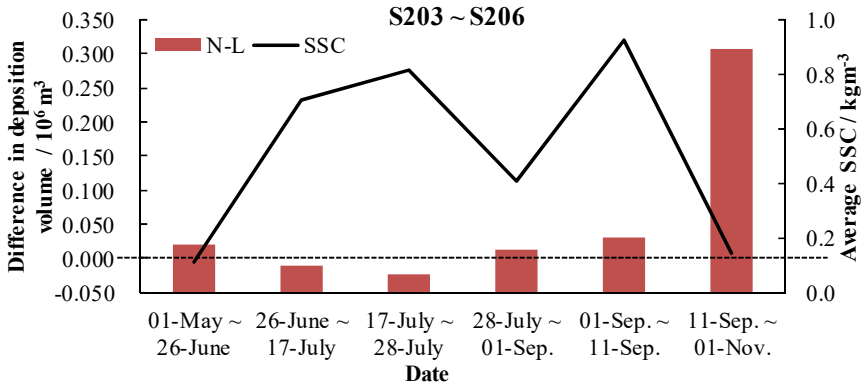

Figure 7. Differences in deposition volume during different periods (Average SSC means the average suspended sediment concentration during each period).

Figure 8 shows the predicted depth gradients (a) and velocity distributions (b) by the L and N models at S206 on June 5 and September 18 (as typical days of the first and last periods) respectively, illustrating the effects of bed topography. It clearly reveals that the velocity redistribution on September 18 is resulted from the bed topography effects as the sediment load on the two days is about 0.1 ~ 0.3 kg·m^{-3}. In all, the low sediment load and the velocity redistribution induced by secondary flow produced by upstream bend and the bed topography result in the difference deposition predictions by the two models.

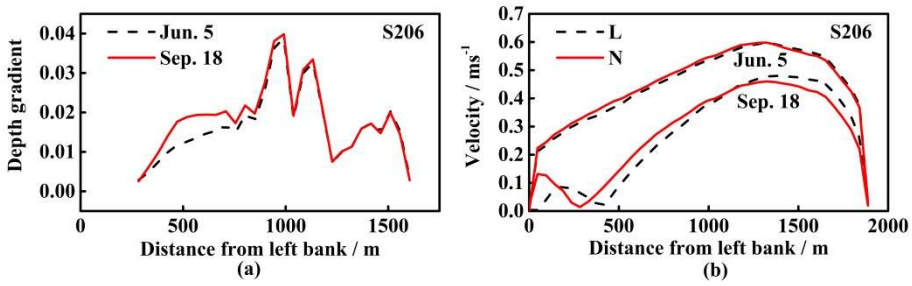

Figure 8. (a) Depth gradient (represents bed topography effects); (b) Velocity distribution predicted by the N and L models at S206 on typical days of the first and last period, respectively.

5. Discussion

One of the most important physical processes in meandering rivers is the outward shifting of main flow velocity caused by secondary flow, which is driven by channel curvature or point bars bed topography [3]. The latter one is called topography-steering [9], which play a significant role in meander dynamics [3]. Whether and how the correction terms representing the secondary flow

effects quantify this process and the performances of these models in meandering channels of different scales will be discussed in this part. Besides, secondary flow effects on the total amount of deposition of the aforementioned part of this reach (S203 ~ S206) are controlled by the properties of cohesive sediment, which will be investigated as well.

5.1. Secondary Flow Effects on Flow Field

5.1.1. Topography Effects

Equation (6) clearly reveals that the correction terms of the three models are directly proportional to the gradients of water depth (H). Due to the effects of bed topography, the longitudinal and transverse gradient of water depth in HHC reach is in the range of 0.01~0.001 and 0.01~0.1, respectively. Therefore the magnitudes of correction terms follow the same tendency as that of the gradients of water depths, in other words, the correction terms are able to reflect the topography effects. Blanckaert [52] has pointed out that only the gravity term can account for the effects of bed topography, and the conventional 2D model (N model) is more suitable for flow simulation in sharply curved bends over developed bed, instead of 2D correction models (e.g. L, NL and B model). However, according to the previous analysis, the effects of bed topography can be reflected by the correction terms to some degree apart from the gravity term. In addition, the simulation results shown in Figure 4 clearly indicate that 2D models that include secondary flow effects (e.g. L model) should be given first priority when it comes to sharp meandering channels with bed topography, such as the HHC reach. This has been confirmed by de Vriend [53] who found that his mathematical model with considering secondary flow effects worked better for curved flow simulation over developed bed.

5.1.2. Applicability of Different Secondary Flow Models

The differences among these models are listed in Table 1, which mainly lie in whether considering the effects of phase lag (B and NL model), sidewall boundary conditions (B model) and bend sharpness (NL model). As the HHC reach is sharply curved bends, the saturation effect considered by the NL model has weakened the secondary flow effects, which result in the minor differences of simulation results between the NL and N models (Figure 4). The depth to width ratio (H/w) distinguishes between meandering channels of different scales. It is approximately 0.001 ~ 0.06 in the HHC reach at the discharge of 30200 m^3/s, while that in the laboratory bend channels and small meandering rivers are in the range of 0.05 ~ 0.25 [44] and 0.06 ~ 0.1 [54] respectively. Therefore, the effects of wall boundary conditions and phase lag have been reduced for such small value of H/w. Although B model has taken the bed topography effects into account in a similar way as the L model does, its correction terms only focus on the longitudinal direction. Consequently, the flow simulation results of the L model are better than that of the B model in the HHC reach. Overall, L model is preferable to flow simulation in meandering channels of mega scale, such as HHC reach. However, for curved bends of laboratory scale, the B model obtains better results [44].

5.2. Secondary Flow Effects on Deposition Amounts

According to the deposition simulation results, secondary flow effects on the total deposition volume are small during an annual hydrograph (Figure 7). However, these effects vary with the changes of the cohesive sediment properties, such as settling velocity and critical shear stresses of cohesive sediment, which depend on the flow conditions and the process of bed consolidation. Series of numerical experiments are designed to investigate secondary flow effects on the deposition volume of cohesive sediment with different properties. And these effects are reflected by the relative difference in deposition amounts (RD) predicted by the N and L models. Numerical experiments are conducted under the same flow condition (Table 3) to keep the strength of secondary flow constant in the HHC reach. The calculation time for each experiment is 33 days. Different properties of cohesive sediment (Table 4) are represented by the variation of settling

velocity (ω_s) and the critical shear stress for deposition (τ_{cd}). Other parameters used in sediment module are the same as that of HHC reach.

Table 4. Settling velocity (ω_s) and critical shear stress for deposition (τ_{cd}) in numerical experiments and results.

ω_s / m/s	RD[1] / %	τ_{cd} / Pa	RD[1] / %
2.1	0.92	0.41	0.92
1.5	3.80	0.44	0.03
1.0	6.38	0.80	-9.36
0.5	9.01	1.00	-10.61

[1] The relative difference in deposition amounts (RD) predicted by N and L models

Calculated RD values are listed in Table 4. It is obtained by calculating the difference of the predicted amounts of deposition by L and N models, and then divided by the N model predictions. The negative value of it means the amount of deposition simulated by the L model is smaller than that by the N model. The relationships of RD against ω_s and τ_{cd} are shown in Figure 9. RD is in reverse linear proportion to ω_s, which means the secondary flow effects on the deposition volume increase with the decrease of settling velocity of cohesive sediment. For τ_{cd} is about 0.44 Pa, RD is approaching zero. It implies that secondary flow nearly has no effect on the total deposition volume while its effects on planar distribution can still exit (Figure 5d). As the τ_{cd} increases, the secondary flow impacts on deposition become greater. In general, RD varies with the settling velocity and critical shear stress for deposition of cohesive sediment and the magnitudes of RD are within 11% based on the parameter values used here.

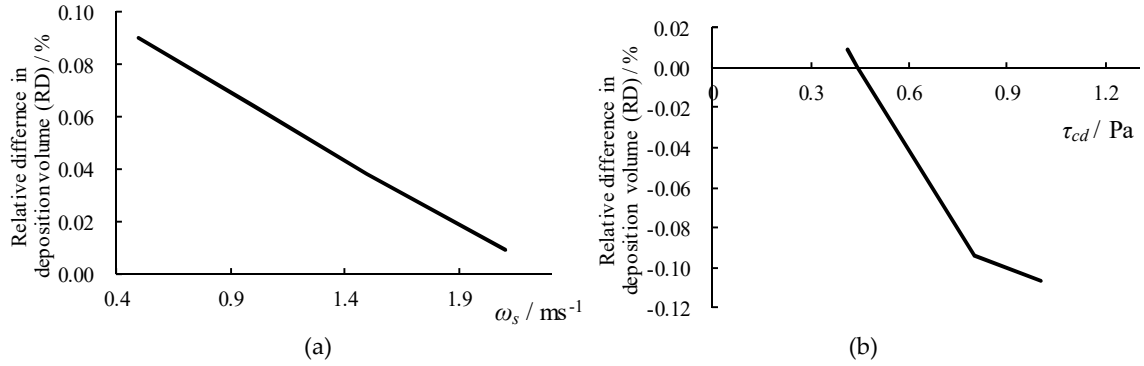

Figure 9. The relationships of relative difference in deposition volume (RD) predicted by the L and N models against (a) Settling velocity (ω_s); and (b) Critical shear stress (τ_{cd}).

5.3. Future Reseach Directions

(1) As the study case is a reach of Yangtze River which belongs to mega rivers, secondary flow effects on bed morphology of meandering channels of different scales (natural rivers with different width to depth ratio) should be investigated. Besides, as the bank of HHC reach is non-erosional, the evolutions of natural rivers with floodplain consisting of cohesive sediment should be simulated by the 2D model developed here. In addition, long-term simulations, such as decadal timescales should be considered in the future to research the cumulative effects of secondary flow.

(2) As to the cohesive sediment transport, the values of parameters play important parts in the distributions and amounts of sediment deposition (Figure 9). The roles they played should be compared with that of secondary flow in bed morphology variations. More importantly, the erosion processes should be studied as these processes cannot be reflected obviously in the HHC reach.

6. Conclusions

In order to investigate secondary flow effects on cohesive sediment deposition in a meandering reach of the Yangtze River, a conventional 2D numerical model (N model) has been improved to

consider different impacts of secondary flow and cohesive sediment transport. The improved 2D model includes three different submodels, that is, Lien (L) model [37] with a wide application in literature, Bernard (B) model [35] considering the phase lag effect and sidewall boundary conditions of secondary flow and a nonlinear (NL) model [1] accounting for the saturation effect of secondary flow in sharp bends. All of the models can reflect velocity redistribution caused by secondary flow to a certain degree. A module for cohesive sediment transport has been coupled into the N model as well. Simulation results are as follows.

(1) In flow calculations, the secondary flow effects on water stage and velocity distribution are well predicted. Velocity redistribution has been reproduced fairly well by the L model in the HHC reach, which means the improved 2D model is able to predict the secondary flow impacts on meandering channels of such mega scale. However, this reach has a small depth to width radio for the discharge of 30200$m^3 \cdot s^{-1}$, thus the effects of phase lag are not obvious. In cohesive sediment deposition simulations, the L model performs better than the N model in planar distribution of deposition, due to more sediment deposit on the concave banks of the bends, which is resulted from the velocity redistribution caused by secondary flow.

(2) The difference in predicted amounts of deposition between the L and N models is evident during the last period of an annual hydrograph when the sediment load is low and the velocity redistribution caused by topography is obvious in this reach.

(3) The topography effects on flow field can be reflected due to the positive relationships between the correction terms of secondary flow submodels and the gradients of water depths, which result in great improvements of velocity predictions of the L model in this reach. Secondary flow effects on predicted amounts of deposition vary with the settling velocity and critical shear stress for deposition of cohesive sediment, and the relative difference of predicted total amounts of deposition by the L and N models is within 11% based on the parameter values used here.

Author Contributions: Conceptualization, C. Q. and X.-J. S.; methodology, C. Q.; software, C. Q.; validation, C. Q.; formal analysis, C. Q.; investigation, C. Q.; resources, Y. X.; data curation, Y. X.; writing—original draft preparation, C. Q.; writing—review and editing, X.-J. S.; visualization, C. Q.; supervision, X.-J. S.; project administration, X.-J. S.; funding acquisition, X.-J. S..

Funding: This research was funded by National Key R&D Program of China (2018YFC0407402-01).

Acknowledgments: Great thanks to Baozhen Jia for her helpful advices and discussion about this paper; Many thanks to Yanjun Wang for the formation of the ideas about this paper.

Conflicts of Interest: The authors declare no conflict of interest.

References

1. Blanckaert, K.; de Vriend, H.J. Nonlinear modeling of mean flow redistribution in curved open channels. *Water Resources Research* **2003**, *39*.
2. Blanckaert, K.; de Vriend, H.J. Meander dynamics: A nonlinear model without curvature restrictions for flow in open-channel bends. *Journal of Geophysical Research* **2010**, *115*, F04011.
3. Camporeale, C.; Perona, P.; Porporato, A.; Ridolfi, L. Hierarchy of models for meandering rivers and related morphodynamic processes. *Reviews of Geophysics* **2007**, *45*.
4. Duan, J.G.; Julien, P.Y. Numerical simulation of the inception of channel meandering. *Earth Surface Processes and Landforms* **2005**, *30*, 1093-1110.
5. Jang, C.-L.; Shimizu, Y. Numerical Simulation of Relatively Wide, Shallow Channels with Erodible Banks. *Journal of Hydraulic Engineering* **2005**, *131*, 565-575.
6. Sun, J.; Lin, B.-l.; Kuang, H.-w. Numerical modelling of channel migration with application to laboratory rivers. *International Journal of Sediment Research* **2015**, *30*, 13-27.
7. Odgaard, A.J.; Bergs, M.A. FLOW PROCESSES IN A CURVED ALLUVIAL CHANNEL. *Water Resources Research* **1988**, *24*, 45-56.
8. Abad, J.D.; Garcia, M.H. Experiments in a high-amplitude Kinoshita meandering channel: 2. Implications of bend orientation on bed morphodynamics. *Water Resources Research* **2009**, *45*.
9. Dietrich, W.E.; Smith, J.D. Influence of the Point Bar on Flow through Curved Channels. *Water Resources Research* **1983**, *19*, 1173-1192.

10. Elina, K.; Petteri, A.; Matti, V.; Hannu, H.; Juha, H. Spatial and temporal distribution of fluvio-morphological processes on a meander point bar during a flood event. *Hydrology Research* **2013**, *44*, 1022-1039.
11. Li, W.; Wang, J.; Yang, S.; Zhang, P. Determining the Existence of the Fine Sediment Flocculation in the Three Gorges Reservoir. *Journal of Hydraulic Engineering* **2015**, *141*, 05014008.
12. Li, W.; Yang, S.; Jiang, H.; Fu, X.; Peng, Z. Field measurements of settling velocities of fine sediments in Three Gorges Reservoir using ADV. *International Journal of Sediment Research* **2016**, *31*, 237-243.
13. Xiao, Y.; Yang, F.S.; Su, L.; Li, J.W. Fluvial sedimentation of the permanent backwater zone in the Three Gorges Reservoir, China. *Lake and Reservoir Management* **2015**, *31*, 324-338.
14. Krone, R.B. *Flume studies of the transport of sedi-ment in estuarial shoaling processes*; Hydraulic Engineering Laboratory: University of California, 1962.
15. De, H.J.; Vriend. Velocity redistribution in curved rectangular channels. *J. Fluid Mech.* **1981**, *107*, 423-439.
16. Johannesson, H.; Parker, G. Velocity Redistribution in Meandering Rivers. *Journal of Hydraulic Engineering* **1989**, *115*, 1019-1039.
17. Blanckaert, K. Saturation of curvature-induced secondary flow, energy losses, and turbulence in sharp open-channel bends: Laboratory experiments, analysis, and modeling. *Journal of Geophysical Research* **2009**, *114*.
18. Johannesson, H.; Parker, G. Secondary Flow in Mildly Sinuous Channel. *Journal of Hydraulic Engineering* **2015**, *115*, 289-308.
19. Nicholas, A.P.; Ashworth, P.J.; Sambrook Smith, G.H.; Sandbach, S.D. Numerical simulation of bar and island morphodynamics in anabranching megarivers. *Journal of Geophysical Research: Earth Surface* **2013**, *118*, 2019-2044.
20. Ashworth, P.J.; Best, J.L.; Roden, J.E.; Bristow, C.S.; Klaassen, G.J. Morphological evolution and dynamics of a large, sand braid-bar, Jamuna River, Bangladesh. *Sedimentology* **2000**, *47*, 533-555.
21. Hackney, C.R.; Darby, S.E.; Parsons, D.R.; Leyland, J.; Aalto, R.; Nicholas, A.P.; Best, J.L. The influence of flow discharge variations on the morphodynamics of a diffluence-confluence unit on a large river. *Earth Surface Processes and Landforms* **2018**, *43*, 349-362.
22. Parsons, D.R.; Best, J.L.; Lane, S.N.; Orfeo, O.; Hardy, R.J.; Kostaschuk, R. Form roughness and the absence of secondary flow in a large confluence–diffluence, Rio Paraná, Argentina. *Earth Surface Processes and Landforms* **2007**, *32*, 155-162.
23. Szupiany, R.N.; Amsler, M.L.; Hernandez, J.; Parsons, D.R.; Best, J.L.; Fornari, E.; Trento, A. Flow fields, bed shear stresses, and suspended bed sediment dynamics in bifurcations of a large river. *Water Resources Research* **2012**, *48*.
24. Szupiany, R.N.; Amsler, M.L.; Parsons, D.R.; Best, J.L. Morphology, flow structure, and suspended bed sediment transport at two large braid-bar confluences. *Water Resources Research* **2009**, *45*.
25. Nicholas, A.P. Modelling the continuum of river channel patterns. *Earth Surface Processes and Landforms* **2013**, *38*, 1187-1196.
26. Rhoads, B.L.; Johnson, K.K. Three-dimensional flow structure, morphodynamics, suspended sediment, and thermal mixing at an asymmetrical river confluence of a straight tributary and curving main channel. *Geomorphology* **2018**, *323*, 51-69.
27. Abad, J.D.; Buscaglia, G.C.; Garcia, M.H. 2D stream hydrodynamic, sediment transport and bed morphology model for engineering applications. *Hydrological Processes* **2008**, *22*, 1443-1459.
28. Guan, M.; Wright, N.G.; Sleigh, P.A.; Ahilan, S.; Lamb, R. Physical complexity to model morphological changes at a natural channel bend. *Water Resources Research* **2016**, *52*, 6348-6364.
29. Iwasaki, T.; Shimizu, Y.; Kimura, I. Sensitivity of free bar morphology in rivers to secondary flow modeling: Linear stability analysis and numerical simulation. *Advances in Water Resources* **2016**, *92*, 57-72.
30. Yang, H.; Lin, B.; Sun, J.; Huang, G. Simulating Laboratory Braided Rivers with Bed-Load Sediment Transport. *Water* **2017**, *9*, 686.
31. Kasvi, E.; Alho, P.; Lotsari, E.; Wang, Y.; Kukko, A.; Hyyppä, H.; Hyyppä, J. Two-dimensional and three-dimensional computational models in hydrodynamic and morphodynamic reconstructions of a river bend: sensitivity and functionality. *Hydrological Processes* **2015**, *29*, 1604-1629.
32. Kang, T.; Kimura, I.; Shimizu, Y. Responses of Bed Morphology to Vegetation Growth and Flood Discharge at a Sharp River Bend. *Water* **2018**, *10*, 223.
33. Reesink, A.J.H.; Ashworth, P.J.; Sambrook Smith, G.H.; Best, J.L.; Parsons, D.R.; Amsler, M.L.; Hardy, R.J.; Lane, S.N.; Nicholas, A.P.; Orfeo, O., et al. Scales and causes of heterogeneity in bars in a large multi-channel river: Río Paraná, Argentina. *Sedimentology* **2014**, *61*, 1055-1085.

34. Begnudelli, L.; Valiani, A.; Sanders, B.F. A balanced treatment of secondary currents, turbulence and dispersion in a depth-integrated hydrodynamic and bed deformation model for channel bends. *Advances in Water Resources* **2010**, *33*, 17-33.
35. Bernard, R.S. *STREMR: Numerical model for depth-averaged incompressible flow*; Hydraulics Laboratory: Waterways Experiment Station, US Army Corps of Engineers, 1993.
36. Duan, J.G. Simulation of Flow and Mass Dispersion in Meandering Channels. *Journal of Hydraulic Engineering* **2004**, *130*, 964-976.
37. Lien, H.C.; Hsieh, T.Y.; Yang, J.C.; Yeh, K.C. Bend-Flow Simulation Using 2D Depth-Averaged Model. *Journal of Hydraulic Engineering* **1999**, *125*, 1097-1108.
38. Song, C.G.; Seo, I.W.; Kim, Y.D. Analysis of secondary current effect in the modeling of shallow flow in open channels. *Advances in Water Resources* **2012**, *41*, 29-48.
39. Jin, Y.-C.; Steffler, P.M. Predicting Flow in Curved Open Channels by Depth-Averaged Method. *Journal of Hydraulic Engineering* **1993**, *119*, 109-124.
40. Abad, J.D.; Garcia, M.H. Experiments in a high-amplitude Kinoshita meandering channel: 1. Implications of bend orientation on mean and turbulent flow structure. *Water Resources Research* **2009**, *45*.
41. Wang, H.; Zhou, G.; Shao, X. Numerical simulation of channel pattern changes Part I: Mathematical model. *International Journal of Sediment Research* **2010**, *25*, 366-379.
42. Hydraulics., W.D. *Delft3D-FLOW User Manual (Version: 3.15.30059): Simulation of multi-dimensional hydrodynamic flows and transport phenomena, including sediments*; Deltares, Ed. Deltares: Rotterdamseweg 185,MH Delft, The Netherlands, 2013; pp. 226-230.
43. HOSODA, T.; NAGATA, N.; KIMURA, I.; MICHIBATA, K.; IWATA, M. A DEPTH AVERAGED MODEL OF OPEN CHANNEL FLOWS WITH LAG BETWEEN MAIN FLOWS AND SECONDARY CURRENTS IN A GENERALIZED CURVILINEAR COORDINATE SYSTEM. In *Advances in Fluid Modeling and Turbulence Measurements*, 10.1142/9789812777591_0007pp. 63-70.
44. Qin, C.; Shao, X.; Zhou, G. Comparison of Two Different Secondary Flow Correction Models for Depth-averaged Flow Simulation of Meandering Channels. *Procedia Engineering* **2016**, *154*, 412-419.
45. Ottevanger, W. Modelling and parameterizing the hydro- and morphodynamics of curved open channels. Doctoral Thesis, Delft University of Technology, the Netherlands, 2013.
46. Gu, L.; Zhang, S.; He, L.; Chen, D.; Blanckaert, K.; Ottevanger, W.; Zhang, Y. Modeling Flow Pattern and Evolution of Meandering Channels with a Nonlinear Model. *Water* **2016**, *8*, 418.
47. Lin, Q.; Wu, W. A one-dimensional model of mixed cohesive and non-cohesive sediment transport in open channels. *Journal of Hydraulic Research* **2013**, *51*, 506-517.
48. Latrubesse, E.M. Large rivers, megafans and other Quaternary avulsive fluvial systems: A potential "who's who" in the geological record. *Earth-Science Reviews* **2015**, *146*, 1-30.
49. Dargahi, B. Three-dimensional flow modelling and sediment transport in the River Klarälven. *Earth Surface Processes and Landforms* **2004**, *29*, 821-852.
50. Kleinhans, M.G.; Jagers, H.R.A.; Mosselman, E.; Sloff, C.J. Bifurcation dynamics and avulsion duration in meandering rivers by one-dimensional and three-dimensional models. *Water Resources Research* **2008**, *44*.
51. Fang, H.-W.; Rodi, W. Three-dimensional calculations of flow and suspended sediment transport in the neighborhood of the dam for the Three Gorges Project (TGP) reservoir in the Yangtze River. *Journal of Hydraulic Research* **2010**, *41*, 379-394.
52. Blanckaert, K. Discussion of "Investigation on the Stability of Two-Dimensional Depth-Averaged Models for Bend-Flow Simulation" by T. Y. Hsieh and J. C. Yang. *Journal of Hydraulic Engineering* **2005**, *131*, 625-628.
53. De Vriend, H.J. A Mathematical Model Of Steady Flow In Curved Shallow Channels. *Journal of Hydraulic Research* **1977**, *15*, 37-54.
54. Wei, M.; Blanckaert, K.; Heyman, J.; Li, D.; Schleiss, A.J. A parametrical study on secondary flow in sharp open-channel bends: experiments and theoretical modelling. *Journal of Hydro-environment Research* **2016**, *13*, 1-13.